Research Square

Preprints are preliminary reports that have not undergone peer review. They should not be considered conclusive, used to inform clinical practice, or referenced by the media as validated information.

Polygonal patterns of cyclones on Jupiter: Convective forcing and anticyclonic shielding

Andrew Ingersoll (api@gps.caltech.edu)
California Institute of Technology https://orcid.org/0000-0002-2035-9198

Shawn P. Ewald
California Institute of Technology

Federico Tosi
Istituto Nazionale di AstroFisica

Alberto Adriani
Istituto Nazionale di AstroFisica

Alessandro Mura
Istituto Nazionale di AstroFisica

Davide Grassi
Istituto Nazionale di AstroFisica

Christina Plainaki
Agenzia Spaziale Italiana

Giuseppe Sindoni
Agenzia Spaziale Italiana

Cheng Li
University of Michigan

Lia Siegelman
Scripps Institution of Oceanography

Patrice Klein
California Institute of Technology

William R. Young
Scripps Institution of Oceanography

Article

Keywords: Jupiter, Juno, vortex, convection, atmosphere

Posted Date: May 11th, 2021

DOI: https://doi.org/10.21203/rs.3.rs-388198/v1

License: This work is licensed under a Creative Commons Attribution 4.0 International License.
Read Full License

Polygonal patterns of cyclones on Jupiter:

Convective forcing and anticyclonic shielding

Andrew P. Ingersoll[a,1], Shawn P. Ewald[a], Federico Tosi[b], Alberto Adriani[b], Alessandro Mura[b], Davide Grassi[b], Christina Plainaki[c], Giuseppe Sindoni[c], Cheng Li[d], Lia Siegelman[e], Patrice Klein[f], William R. Young[e]

[a]Planetary Science, California Institute of Technology, 1200 E. California Blvd, Pasadena, CA 91125, USA

[b]Istituto Nazionale di AstroFisica – Istituto di Astrofisica e Planetologia Spaziali (INAF-IAPS), Rome, Italy

[c]Agenzia Spaziale Italiana (ASI), Via del Politecnico snc, 00133 - Rome, Italy

[d]Climate and Space Sciences and Engineering, University of Michigan, 2455 Hayward Street, Ann Arbor, MI 48109, USA

[e]Scripps Institution of Oceanography, University of California, San Diego, La Jolla, CA 92037, USA

[f]Environmental Science and Engineering Department, Geological and Planetary Sciences Division, CALTECH, 1200E California Blvd, Pasadena CA 91125, USA

[1]**Corresponding author:** Andrew P. Ingersoll, 626-376-6872, api@gps.caltech.edu

ORCIDS registered at PNAS by individual authors

Author Contributions: API led the research and wrote the document. SPE did the data analysis and prepared the figures. FT prepared the geometric tables that were used in the analysis. Others oversaw the successful functioning of the JIRAM instrument and provided expertise on using it for image processing. CL, LS, PK and WRY provided expertise on vortices.

Competing Interest Statement: No competing interests

Keywords: Jupiter, Juno, vortex, convection, atmosphere

This PDF file includes:

Main Text: Introduction, Results, Discussion, Methods
Figures 1 to 4
Tables: none

Abstract

From its unique pole-to-pole orbit, the Juno spacecraft discovered cyclones arranged in polygonal patterns around the poles of Jupiter. In a related modeling study the stability of the pattern depends on shielding -- a ring of anticyclonic vorticity surrounding each cyclone. Without shielding the vortices merge. Here we present high-resolution measurements obtained by tracking clouds in sequences of infrared images. There is vorticity of both signs at 200-km scales. The standard deviation is 0.32 times the vorticity of a large cyclone, whose relative vorticity is 0.46 times the planetary vorticity. Shielding exists at large scales, and it has the magnitude and distance from the vortex center predicted in the model. There is horizontal divergence of both signs at 200-km scales, with standard deviation 0.64 times the vorticity standard deviation. We propose that these intense structures are convection and that convection is the principal energy source for the large vortices.

Significance Statement

Vorticity is the local rate of spin. For large-scale, slowly-varying flows in atmospheres and oceans, the spin of the planet is greater than that of the flow and is therefore a controlling factor. The vortices at Jupiter's poles are particularly interesting because they are arranged in geometric patterns that endure for years. Such patterns have been seen in laboratory experiments and theoretical models but never before in a planetary atmosphere. With a 10-fold increase in spatial resolution, we have discovered a world seething with intense small-scale activity. The interaction of this world with the large vortices resembles a food chain, with convection bringing energy up from below. Studying these exotic atmospheric structures helps us understand vortex behavior in general.

At Jupiter's north pole there are eight cyclones that form an octagon, with one cyclone at each vertex and one additional cyclone in the center [1 2]. The centers of the cyclones are at latitudes of $83 \pm 1°$, which is about 8700 km from the pole. Jupiter's south pole is the same except there are only five cyclones that form a pentagon and one at the center, with vertices at latitudes of $-83 \pm 1°$. The polygons and the individual vortices that comprise them have been stable for four years of observation [34]. The observations are taken every 53 days over a 1-2 hour period at perijove, which is the spacecraft's closest approach to Jupiter. The peak azimuthal wind speeds around each vortex range from 70 to 100 m s^{-1}, and the radial distance from the peak to the vortex center is about 1000 km [5]. The polygonal patterns rotate slowly, such that the vertices in the south drift to the west at 0.04 m s^{-1} and those in the north show no consistent drift [3]. The cyclones perform small regular oscillations, but neither the merging nor the disappearance of any cyclone has occurred[6].

There have been only a handful of theoretical studies that specifically address the polar cyclones on Jupiter and Saturn [7 8 9 10 11]. Saturn's polar cyclones are fundamentally different from Jupiter's because there is only one at each pole [12 13]. Moreover, Saturn has a 160 m s^{-1} zonal jet located at a latitude of $-88.5°$ circling the south pole [14]. Saturn's north pole has not been measured. In contrast, there are no zonal jets greater than 10 m s^{-1} circling the poles of Jupiter [15]. Saturn's northern hemisphere has a hexagon, which is a meandering zonal jet at 75° whose six excursions in latitude give it a hexagonal shape [16 17 18 19 20]. But the hexagon has no closed-streamline structures, i.e., no vortices, and exists by a different mechanism from the polar cyclones on Jupiter.

In a related modeling paper with some of the same authors, Li20[7], we created cyclones that have the observed gross properties - maximum velocity and radius, and arranged the cyclones into polygonal patterns around the pole to see which ones are stable. This approach reveals the importance of shielding – a ring of anticyclonic vorticity surrounding each of the cyclones. Shielding is important in tropical meteorology. It determines whether tropical cyclones merge, drift apart, or orbit each other [21222324]. In Li20 the radius of the anticyclonic ring divided by the radius of maximum cyclonic velocity must be less than 4.5 in order to get a stable pattern[7]. A larger ratio leads to merging and ultimately a single polar cyclone. Anticyclonic vorticity is present in the models discussed earlier [891011], but apparently it does not organize into shields that are strong enough to prevent merging.

In the present paper our measurement objective was to measure the velocity throughout the north polar region at scales down to ~100 km. From the velocity field we would compute the vertical component of vorticity and horizontal divergence. One goal was to look for shielding to see if the theory of Li20 might apply to Jupiter. The other goal was simply to explore the hidden world of small-scale motions. We found shielding, but we also discovered a world where horizontal divergence and convergence rivaled the vorticity, and vorticity of both signs rivaled that of the large-scale cyclones.

Scales of the Motion

The vertical component of vorticity due the planet's spin is $2\Omega\cos\theta$ and is called f, the planetary vorticity, where Ω is the planetary rotation rate and θ is colatitude. The increase of f

with northward distance, $df/dy = 2\Omega\sin\theta/a$ is called β, where a is the radius of the planet. On Earth it causes cyclones to drift poleward[21,22]. An important length scale at mid-latitudes is $L_\beta = (V/\beta)^{1/2}$, where V is a characteristic velocity. It roughly matches the widths of the zonal jets on Jupiter and Saturn[25,26,27,28]. The length scale enters in criteria for zonal jet stability [29], and it is also the scale below which the flow is dominated by turbulence and above which it tends toward alternating zonal jets. With small-scale vortices as an initial condition, the flow evolves through a state of propagating waves and then tends toward alternating zonal jets[30]. However, at the poles, where β tends linearly to zero, a length scale based on minus its gradient $\gamma = -d\beta/dy = 2\Omega/a^2$ is more appropriate. The length scale is $L_\gamma = (V/\gamma)^{1/3}$, and for V = 80 m s^{-1} it is about 10,500 km. L_γ represents the radius of the circle around the pole inside of which the effect of the vortices - turbulence -- is greater than the effect of β and the jets. Note that L_γ is the distance from a specific point -- the pole, and L_β is not. The value of L_γ is close to the 8700 km size of the polygons on Jupiter.

The effect of deep winds on surface features is uncertain. The Juno gravity field indicates that the zonal winds extend from the surface down to the 3000 km level[31]. This statement only applies within $\pm 25°$ of the equator, because the gravity wind experiment is not sensitive to higher latitudes[32]. And models of the deep winds show how they might affect the visible features [33,34]. But when one is varying parameters to fit data about specific features, it is wise to start simply. The shallow water (SW) equations have only two dependent variables, the horizontal velocity $\boldsymbol{v}$ and the gravitational potential ϕ associated with the layer thickness, and they are functions only of the horizontal coordinates and time. A single layer of fluid of thickness h that floats hydrostatically on a much thicker fluid at rest is known as a 1.5-layer model. For this we have $\phi = g_r h$, where g_r is the reduced gravity -- the gravitational acceleration times the fractional density difference $\Delta\rho/\rho$ between the two layers [21,22]. ϕ obeys the 2D continuity equation, and minus its horizontal gradient is the acceleration due to pressure. Potential vorticity (PV) is an important conserved quantity–a constant for each fluid element. For the SW equations PV is $(\zeta + f)/\phi$, where $\zeta = (\boldsymbol{\nabla} \times \boldsymbol{v}) \cdot \hat{\boldsymbol{k}}$ is the relative vorticity -- the curl of the horizontal velocity.

Rotation is dominant when the Rossby number $Ro = V/(fL)$ is small, where L is a characteristic length. For a jovian cyclone with V = 80 m s^{-1} and L = 1000 km, one finds Ro = 0.23. The ratio ζ/f is exactly twice this value. The radius of deformation $L_d = \sqrt{\phi}/f$ is the horizontal length scale over which the vortices interact. L_d is inversely proportional to the sine of latitude through the $1/f$ factor, and different assumptions about the vertical stratification put the average L_d at the poles in the range 350 - 1300 km[7]. This brackets the 1000-km radius of the

individual cyclones on Jupiter. If the velocity is fixed, *Ro* increases as *L* decreases, and eventually rotation will not dominate the flow.

Observations

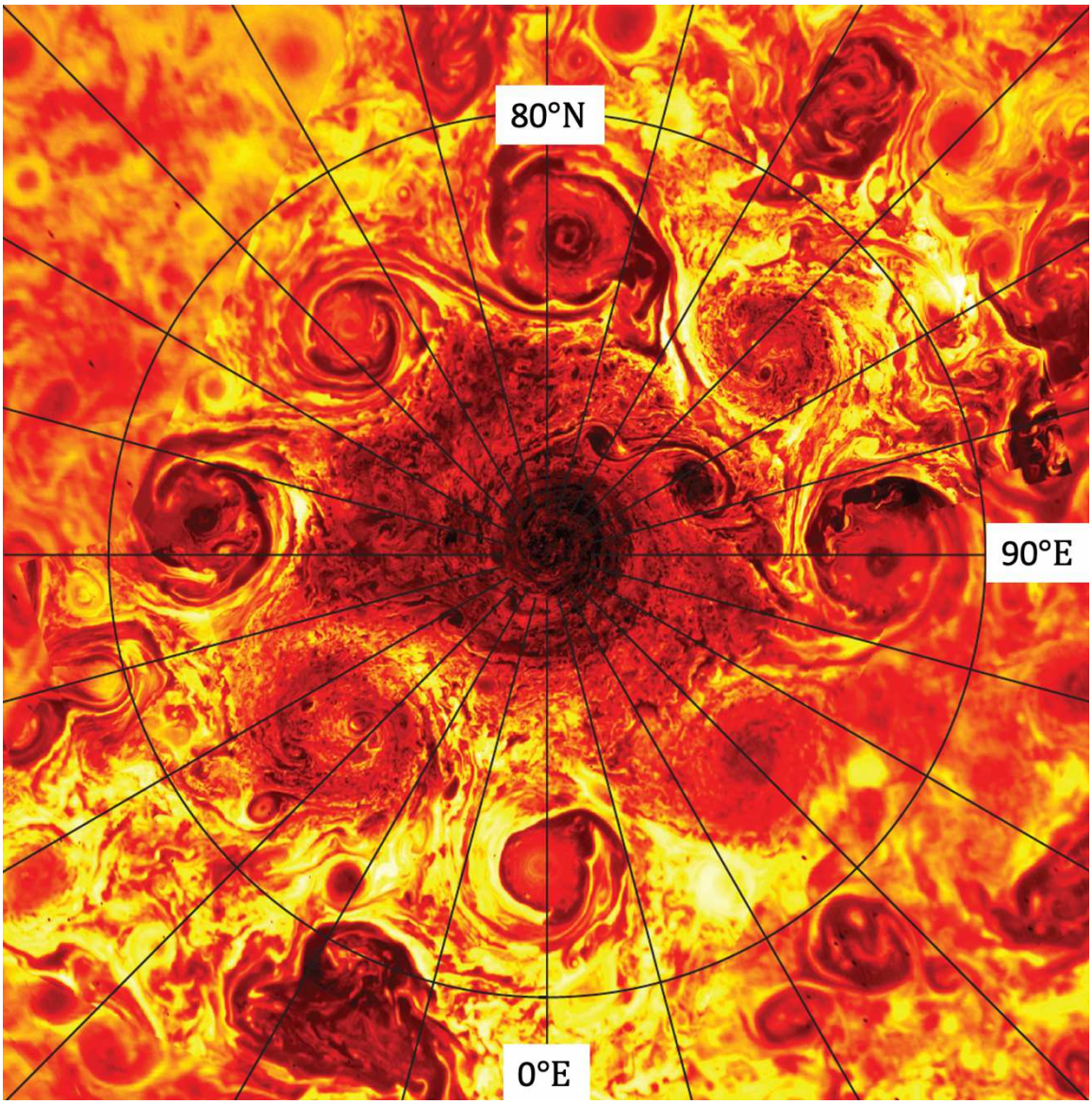

Figure 1. Infrared image of the northern hemisphere as seen by JIRAM [2]. The circle at 80° latitude is about 12,000 km from the pole. The radiances have been corrected for nadir viewing, with bright yellow signifying greater radiance and dark red signifying lesser radiance. Because of these corrections and the non-linearity of the Planck function, one can only say that the average brightness temperature is somewhere in the range 215-220 K. The figures shown in this paper cover the central cyclone and the two cyclones at 135° and 315° east longitude, respectively. The two dark features at 120-150° east, whose filaments spiral toward their centers in a clockwise direction, are anticyclones.

Figure 1 shows the octagon of cyclones surrounding the north pole and describes the region covered by our vorticity and divergence maps. The maps show features in the clouds at scales down to ~100 km, which is much less than the 1000-km radius where the azimuthal velocity is greatest. The measurement requires tracking clouds in a pair of images separated in time to get velocity, and then taking closed line integrals to get vorticity and divergence. The maps are derived from infrared images taken by the Jupiter Infrared Auroral Mapper (JIRAM) on February 2, 2017[35]. The JIRAM M filter tracks the clouds at 4.5-5.0 μm wavelength. A brightness anomaly indicates a hole in the upper cloud, allowing radiation from warmer, deeper levels to escape. Details of image processing are in the Methods section and in the Supplementary Information (SI).

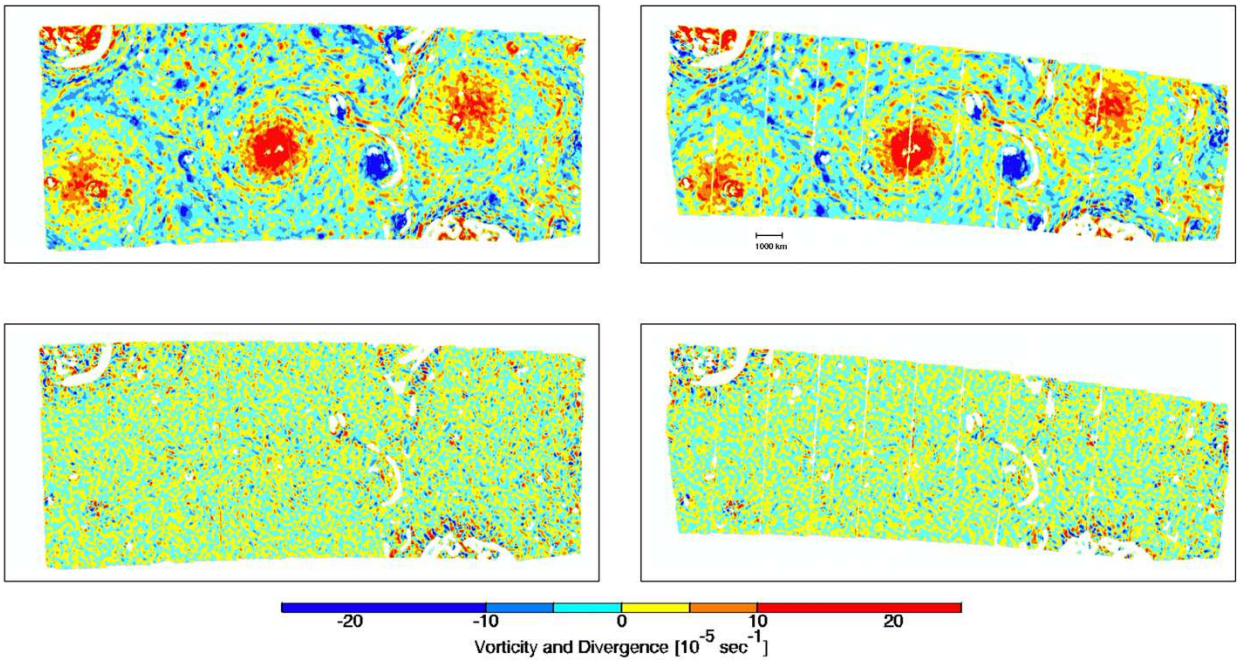

Figure 2. Vorticity (top row) and divergence (bottom row) derived from two determinations of the wind field using separate data (left and right), termed n0103 and n0204. The long dimension of each rectangle is ~20,000 km, and the smallest features are ~100 km in diameter. Each determination is derived from a series, each of which consists of 12 adjacent images laid side by side. The seams between the 12 images are visible as faint vertical lines. The white spaces are regions where the image entropy[36] was below a threshold needed for reliable cloud-tracked wind analysis. They cover 1.8% and 2.1% of the pixels in the left and right maps, respectively. For further information, see the Methods section

Figure 2 shows vorticity and divergence maps for two determinations of the wind field. A series of 12 images was started every 8 minutes to cover the same region at the north pole of Jupiter. The spacecraft was approaching Jupiter, and the image resolution changed from 22 km/pixel in the middle of the first series to 14 km/pixel in the middle of the fourth series, 24 minutes later. The two maps on the left were made by measuring cloud displacements between the first and third series, which are 16 minutes apart, and the two maps on the right were made from the second and fourth series, which are also 16 minutes apart. The left and right maps are separated in time by only 8 minutes, but they use entirely different images. The persistence and

movement of features, even those ~100 km in size, shows that the high-contrast, small-scale features are not measurement noise.

The small features move counterclockwise around the large cyclones and clockwise around the two anticyclones. This motion is visible when one blinks the left and right vorticity maps back and forth, as one can do with *fig_s1_polar_vortex_blink* in the SI. Even at the fastest speed, 80 m s^{-1}, the displacement over 8 minutes is only 38 km, which is ~2 times the resolution of the instrument. Notice that the central cyclone and the two cyclones at lower left and upper right almost disappear in the divergence maps, but the cyclones at upper left and lower right do not. The latter two cyclones are at 90° and 270°E in Figure 1. Their distinguishing characteristic is a lack of small-scale features, which are needed for accurate feature tracking. We used image entropy (Shannon entropy)[36] to confirm this visual impression, and chose an entropy threshold that covered up most but not all of the suspicious pixels in the divergence maps. Those pixels were not used either in the divergence or the vorticity data processing. The original images without the covering and histograms of the entropy are *fig_s2_entropy_masks_removed* in the SI.

Figure 3 shows histograms of the points in Figure 2 and the percentages in each color bin. The standard deviations of vorticity and divergence are 5.1 and 3.25 x 10^{-5} s^{-1}, respectively, but they have longer tails relative to the center than a normal distribution. The long tail of positive vorticity comes mostly from the central cyclone and extends out at least halfway to the planetary vorticity value $f = 2\Omega = 35 \times 10^{-5}$ s^{-1}. The long tail of negative vorticity comes mostly from the two anticyclones to the right of the central cyclone, but there are many smaller features with both positive and negative vorticity. The mean vorticity and mean divergence are 0.02 and 0.23, both in units of 10^{-5} s^{-1}, respectively. Thus the mean values are much less than the standard deviations.

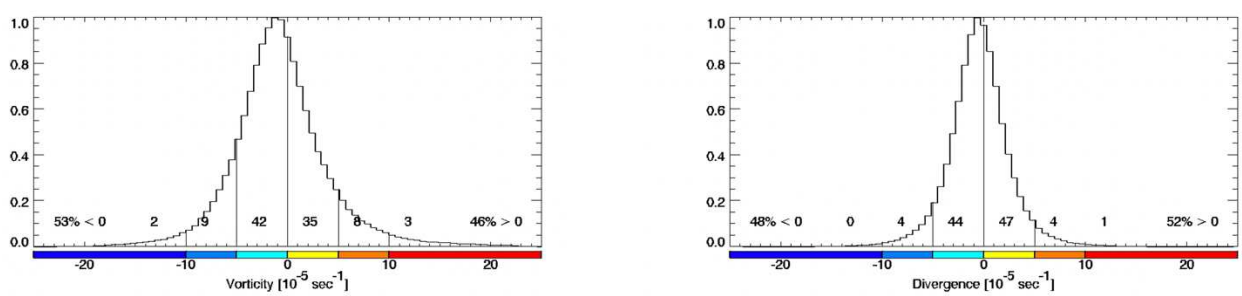

Figure 3. Histograms of vorticity (left) and divergence (right) for the maps shown in Figure 2. The vorticity and divergence scales are the same, and the colors are the same as those used in Figure 2. The number above each color bin is the percentage of pixels in that bin.

Figure 4 shows the azimuthal mean $\bar{v}$ of the azimuthal velocity around the north central cyclone as a function of radius r out to 6000 km. Also shown are the mean vorticity $\bar{\zeta}$, the mean potential $\bar{\phi}$, and the mean potential vorticity $\overline{PV}$. The curves are derived by a linear least squares fit to 5 smooth functions. Therefore they filter out the intense 100-km scale motions without affecting the description of motions on the scale of the cyclones and the region between them. The profile of $\bar{v}(r)$ agrees with earlier estimates[53], including the fact that the profile at $r > 2000$ km falls off faster than $1/r$, implying negative vorticity in that region. See Methods for details on the fitting process.

The profile of azimuthal velocity vs. radius yields a lower bound on the mean radius of deformation $L_d = \sqrt{\phi}/f$. The potential ϕ in Figure 4 is computed from an integral and is therefore uncertain by an additive constant. However, $\phi = g_r h$ is proportional to the thickness, and the thickness cannot be negative. The figure is computed with $\phi = 0$ at the vortex center. The largest ϕ is 69,349 m^2/s^2 at r = 4075 km, and it cannot be smaller there without ϕ becoming negative at the center. This gives $L_d = \sqrt{\phi}/f$ = 749 km as the lower bound for the radius of deformation, which is in the middle of estimates obtained from lower latitudes [7] taking into account the variation of f with latitude. We caution, however, that L_d is a fixed atmospheric parameter only for quasi-geostrophic (QG, or small Rossby number) motion, and Jupiter's polar cyclones are not fully QG, since $\zeta/f \sim 0.46$. In the shallow water equations, L_d describes the stratification far from any strong vortices and large pressure gradients.

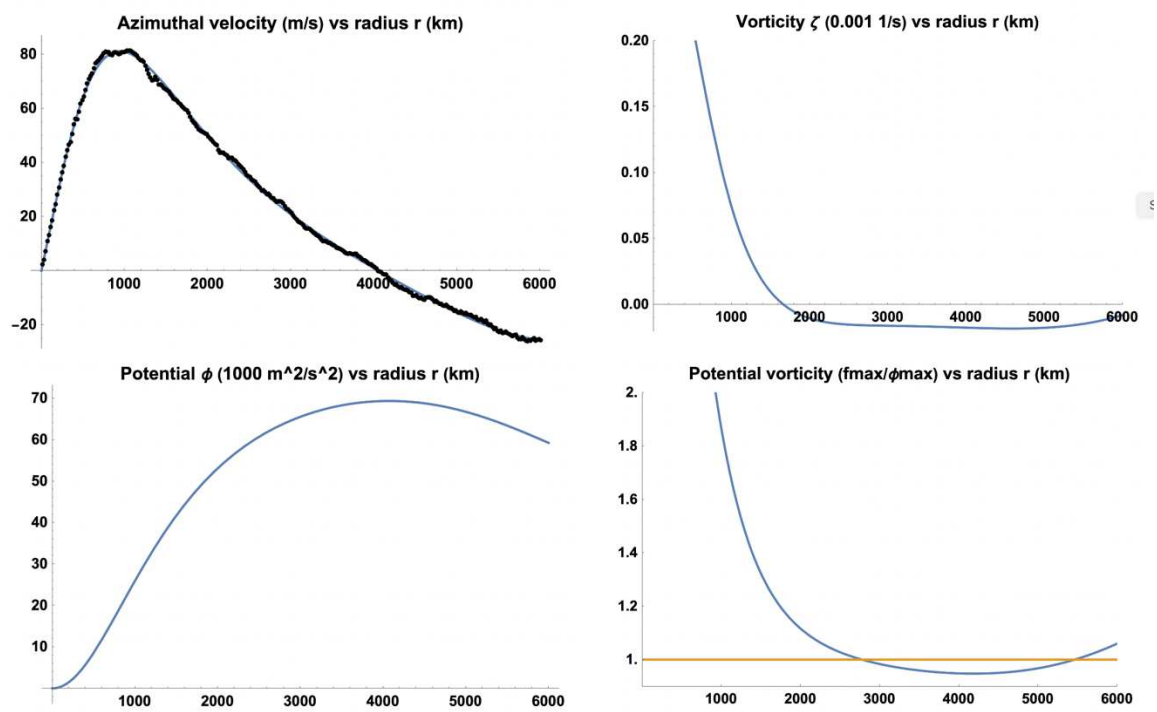

Figure 4. Mean azimuthal velocity and vorticity (top row) and mean gravitational potential and potential vorticity (bottom row). The fitted curve for velocity (blue) is almost covered by the data points (black). Potential vorticity is scaled by the planetary vorticity at the pole divided by the r = 4075 km peak value of ϕ, assuming it is equal to $L_d^2 f^2$ with L_d = 1000 km. The variations of PV are not due to f, which decreases by only 0.35% from the pole to r = 6000 km.

To have stable polygons, Li20 requires an anticyclonic ring - shielding - around each cyclone [7]. The distance from the center of each vortex to the annulus of minimum PV has to fall between ~2 and 4.5 times the radius of maximum azimuthal velocity, which is ~1000 km. Recall that the vertices of the polygons average 8700 km from the pole. Figure 4 shows a broad annulus of negative vorticity at 1600 < r < 6000 km with a minimum of -1.83 x 10^{-5} s^{-1} at r = 4591 km.

This is more than 5% of the planetary vorticity f at the pole but of opposite sign. The scaled PV has a local minimum of 0.948 at r = 4184 km. This minimum is 2 or 3 times deeper than that required by the model. The location of these minima agrees well with the model's ratio of 4.5 for the minimum PV radius to the 1000-km radius of maximum velocity. All of this suggests that large-scale shielding exists on Jupiter and is operating despite the small-scale activity.

Convection

A major scientific result of this paper is the large magnitude of vorticity and divergence with both positive and negative sign at ~200 km scales. These properties point to convection, but not the type of convection observed at lower latitudes. Severe thunderstorms on Earth have diameters of 30-40 km[37,38]. A hurricane is ~20 times larger [39]. But the atmospheric scale height on Jupiter is 5 times larger than on Earth, 40 km vs 8 km. So if the ratio of horizontal to vertical dimensions is the same on the two planets, then jovian thunderstorms should have diameters of 150-200 km. This roughly matches the intense small-scale structures reported in this paper.

Divergence and convergence also point to convection. Horizontal divergence requires vertical convergence and therefore vertical winds, which are defining elements of convection. If a rising parcel conserves PV, then when it spreads out at the top of the atmosphere its $\zeta + f$ must decrease along with its h. Since f is a large positive quantity when the Rossby number is small, and does not change as the parcel rises, the parcel's ζ must decrease by a large fractional amount. In other words, rising parcels become anticyclones when they spread out at the top [40]. The opposite is also true: Upper-level convergence, which would accompany sinking parcels, would lead to cyclonic vorticity at the top of the downwelling plume. The former describes convection in Earth's atmosphere, where moist plumes rising from Earth's boundary layer occupy ~1% of the area and slow sinking occupies the rest [40]. The latter describes convection in Earth's oceans, where cold sinking plumes break out of the mixed layer at the top of the ocean and sink [41]. Lacking a solid surface below the clouds, Jupiter's atmosphere might have both intense updrafts and intense downdrafts,, which is consistent with equal amounts of divergence of both signs. In other words, Jupiter's atmosphere might be behaving partly like an ocean [4].

The ratio of divergence to vorticity at 150-300 scales also points to convection. In units of 10^{-5} s^{-1}, the vorticity standard deviations are 5.1, both for images n0103 and n0204. The corresponding divergence standard deviations are 3.4 and 3.1. The smaller values associated with n0204 are probably due to the 20% better resolution of n0204 compared to n0103. For the large-scale, slowly-varying cyclones compared to the planetary rotation (small Rossby number), one expects small values for the ratio of divergence to vorticity, in any case no larger than ζ/f, which is ~0.46. This upper bound is based on terms in the vorticity equation. Intense, short-lived convection like a terrestrial thunderstorm can have large convergence at the bottom and large divergence at the top. Apparently the small structures that we see in Figures 2 and 3 are intermediate between rotation-dominated and convection-dominated storms.

Although the large divergence suggests convection, the small-scale features in Figs. 2 do not look like the lightning storms at lower latitudes, and both are obvious candidates for convection. The imaging system on Galileo was able to pinpoint the sources of lightning by following the clouds from day to night [42,43] over a 2-3 hour period. The storms range from 200 to

1600 km in size, are separated by 10^4 km in distance, and flash many times per minute. The storms occur overwhelmingly in the belts, which are the cyclonic bands as defined by the alternating eastward and westward jet streams. This seems to contradict evidence for upwelling in the anticyclonic zones[44]. The preference for belts could be due to thinning of the stably stratified upper layers, which brings moisture-laden air up to its lifting condensation level [4546]. Upwelling in the belts at cloud base and downwelling just below the tropopause is a real possibility and an active area of study[474849]

Discussion

What to do next? On the observation side, we will pursue the brightness power spectrum vs. spatial scale and the covariances of vorticity, divergence, and infrared brightness. The latter has a resolution of ~16 km, and the derived divergence and vorticity have a resolution of ~100 km. Low brightness is an indicator of high clouds, which could be a sign either of upward velocity or upward displacement. That effort is a separate paper and has been submitted[50]. We will study Jupiter's white ovals, which also have been observed by JIRAM [51]. On the theory side, one should revisit the polar vortex models that are forced by small-scale convection [891011]. Although lacking a beta effect, there are models that produce large scale vortices from small-scale convection in rapidly-rotating fluids [5253], and that too should be pursued.

Methods

Table S1 in the SI gives the archival filenames and our working names for the 48 images that were used in the analysis. The images are adjacent rectangular strips with 12 images per series, and there are 4 series named n01 to n04, each of which records roughly the same place on the planet 8 minutes after the one before. The size of each resolution element varies smoothly from ~22 km/ pixel in the middle of n01 to ~14 km/pixel in the middle of n04. The first step in the processing is to determine the precise location on the planet of each resolution element in every image. This is done with NAIF/SPICE data from the spacecraft[54] and precise geometric calibration of the JIRAM instrument [35]. The second step is to map the brightness patterns onto a grided reference plane tangent to the planet at the pole. That data is filename *data_s3_mapped brightness* as part of the Supplementary Information (SI).

The third step is to measure cloud displacements in the reference plane using the Tracker3 software from JPL. The software automatically searches for the best correlation of brightness patterns between two images. This is done between images in series n01 and n03 and between images in series n02 and n04. Velocity is the displacement in km divided by the time interval, which is always close to 16 minutes but depends on which image in each series was used. Correlation is done within a square box in the reference plane. After experimenting we settled on 15 km/pixel in the reference plane and a 15 x 15 pixel correlation box for the Tracker3 software. In other words, we use a square 225 km on a side to define a feature. Therefore the resolution of the wind measurement is ±112.5 km. We oversample it by a factor of 2.5 to obtain wind vectors on a 45 x 45 km grid. That data set is filename *data_s4_velocity vectors* in the SI. Finally, we determine vorticity and divergence at every grid point by integrating around the 8

surrounding points using Stokes's theorem and Gauss's law, respectively. Those data are filename *data_s5_figure_2_data* in the SI.

The error in the velocity estimate σ_v depends crucially on the granularity of the scene at the scale of the resolution element δ, which on average is about 18 km. Except for no features at all, for which there is no estimate, the worst case is a single cloud feature of size $\leq \delta$, for which the variance $\sigma_v^2 = 2\delta^2/\Delta t^2$, where Δt is the 16-minute time step and the factor of 2 arises because we are subtracting position in two images. Then $\sigma_v = 2^{1/2}\delta/\Delta t$, about 26.5 m/s. However if the velocity measurement is the average of N statistically independent estimates of velocity, the variance is $2\delta^2/\Delta t^2/N$. The best case is when N is the number of resolution elements in the correlation box, which is L on a side such that $N = (L/\delta)^2$. Then $\sigma_v = 2^{1/2}\delta/\Delta t/N^{1/2} = 2^{1/2}\delta^2/L/\Delta t$, which is 2.1 m/s for L = 225 km.

A quantitative measure of granularity is image entropy H [36]. We define it for each 15 x 15 correlation box from the histogram of brightness values in the box:

$$H = -\sum p_k log_2(p_k) \qquad (1)$$

The input data are 32-bit numbers, but we only have 225 pixels. We divide the range from the brightest to the darkest pixel into 256 grey levels, and we count the number of times that each grey level appears in the image. That number divided by 225 is p_k, the frequency of occurrence of grey level k normalized so that $\sum p_k = 1$. The sum is over the 256 grey levels. If the brightness corresponding to a particular grey level k1 does not occur in the image, then $p_{k1} = 0$. At least 31 of the p_k's must be zero. If all 225 pixels have brightness corresponding to grey level k2, then $p_{k2} = 1$ and all the other p_k's = 0, resulting in $H = 0$. If the brightness levels of all the 225 pixels are different, then $H = log_2(225) = 7.81$. This is the maximum entropy for this problem. Low entropy is bad for feature tracking, and we experimented to find a value that eliminated the most suspicious data, like the large pixel-to-pixel variations in the upper left and lower right corners of the divergence maps. We manually verified that the feature-tracking software was failing in those regions.

The data of Figure 4 consist of ~26,000 measured velocity vectors on the 45 x 45 km grid for radius r from the vortex center < 6010 km. Taking the azimuthal component of each vector, and knowing its r, we did two separate least squares fits, in both cases for the five a_n coefficients in Eq. (2), to get analytic expressions for $\partial\bar{\phi}(r)/\partial r$ and $\bar{v}(r)$, respectively.

$$\frac{\bar{v}^2}{r} + 2\Omega\bar{v} = -\frac{\partial\bar{\phi}}{\partial r}, \qquad \bar{\zeta} = \frac{\partial(r\bar{v})}{r\ \partial r}, \qquad \bar{v} = \sum_1^4 a_n r^n + \frac{a_5 r}{(r^2+r_0^2)} \qquad (2)$$

For a good fit, the parameter r_0 must be close to the radius of the velocity maximum. It was chosen to be 1060 km for $\partial\bar{\phi}/\partial r$ and 1200 km for $\bar{v}$. We analytically integrated the expression for cyclostrophic balance starting from $\bar{\phi} = 0$ at r = 0 to get $\bar{\phi}(r)$ in Figure 4, and we analytically differentiated the expression for velocity to get $\bar{\zeta}(r)$. See the SI for details.

Acknowledgments

This research was carried out at the California Institute of Technology under a contract with the National Aeronautics and Space Administration (NASA), Grant/Cooperative Agreement Number 80NSSC20K0555, and a contract with the Juno mission, which is administered for NASA by the Southwest Research Institute. CL was supported by the 51 peg b Postdoctoral Fellowship. JIRAM was supported by the Italian Space Agency through ASI-INAF agreements n. I/010/10/0, 2014-050-R.0, 2016-23-H.0 and 2016-23-H.1-2018. AA, AM, DG, and FT were supported by INAF. CP and GS were supported by ASI. LS is funded by the Scripps Institution of Oceanography Postdoctoral Fellowship.

Data Availability

JIRAM data are available at the Planetary Data System (PDS) online (https://pds-atmospheres.nmsu.edu/data_and_services/atmospheres_data/JUNO/jiram). Data products used in this report include: calibrated, geometrically controlled, radiance data mapped onto an orthographic projection centered on the north pole; velocity vectors derived from the radiance data; and vorticity and divergence maps derived from the velocity data. These data products, about 150 Mb in volume, are part of the SI.

References

1. Orton, G. S. *et al.* The first close-up images of Jupiter's polar regions: Results from the Juno mission JunoCam instrument. *Geophys. Res. Lett.* **44**, 4599–4606 (2017).
2. Adriani, A. *et al.* Clusters of cyclones encircling Jupiter's poles. *Nature* **555**, 216-+ (2018).
3. Tabataba-Vakili, F. *et al.* Long-term tracking of circumpolar cyclones on Jupiter from polar observations with JunoCam. *Icarus* **335**, UNSP 113405 (2020).
4. Adriani, A. *et al.* Two-year observations of the Jupiter polar regions by JIRAM on board Juno. *J. Geophys. Res.* (2020) doi:DOI: 10.1029/2019JE006098201.
5. Grassi, D. *et al.* First Estimate of Wind Fields in the Jupiter Polar Regions From JIRAM-Juno Images. *J. Geophys. Res.-Planets* **123**, 1511–1524 (2018).
6. Mura, A., Adriani, A. & Bracco, A. Oscillations and stability of the Jupiter polar cyclones. *Nature Astronomy* (2021).

7. Li, C., Ingersoll, A. P., Klipfel, A. P. & Brettle, H. Modeling the stability of polygonal patterns of vortices at the poles of Jupiter as revealed by the Juno spacecraft. *Proc. Natl. Acad. Sci. U. S. A.* **117**, 24082–24087 (2020).
8. Scott, R. K. Polar accumulation of cyclonic vorticity. *Geophys. Astrophys. Fluid Dyn.* **105**, 409–420 (2011).
9. O'Neill, M. E., Emanuel, K. A. & Flierl, G. R. Polar vortex formation in giant-planet atmospheres dues to moist convection. *Nature Geoscience* **8**, 523-U118 (2015).
10. O'Neill, M. E., Emanuel, K. A. & Flierl, G. R. Weak Jets and Strong Cyclones: Shallow-Water Modeling of Giant Planet Polar Caps. *J. Atmos. Sci.* **73**, 1841–1855 (2016).
11. Brueshaber, S. R., Sayanagi, K. M. & Dowling, T. E. Dynamical regimes of giant planet polar vortices. *Icarus* **323**, 46–61 (2019).
12. Orton, G. S. & Yanamandra-Fisher, P. A. Saturn's Temperature Field from High-Resolution Middle-Infrared Imaging. *Science* **307**, 696–698 (2005).
13. Dyudina, U. A. *et al.* Dynamics of Saturn's south polar vortex. *Science* **319**, 1801–1801 (2008).
14. Dyudina, U. A. *et al.* Saturn's south polar vortex compared to other large vortices in the Solar System. *Icarus* **202**, 240–248 (2009).
15. Hueso, R. *et al.* Jupiter cloud morphology and zonal winds from ground-based observations before and during Juno's first perijove. *Geophys. Res. Lett.* **44**, 4669–4678 (2017).
16. Sommeria, J., Meyers, S. & Swinney, H. Laboratory Model of a Planetary Eastward Jet. *Nature* **337**, 58–61 (1989).
17. Allison, M., Godfrey, D. & Beebe, R. A Wave Dynamic Interpretation of Saturns Polar Hexagon. *Science* **247**, 1061–1063 (1990).
18. Aguiar, A. C. B., Read, P. L., Wordsworth, R. D., Salter, T. & Yamazaki, Y. H. A laboratory model of Saturn's North Polar Hexagon. *Icarus* **206**, 755–763 (2010).

19. Sanchez-Lavega, A. *et al.* The long- term steady motion of Saturn's hexagon and the stability of its enclosed jet stream under seasonal changes. *Geophysical Research Letters* **41**, 1425–1431 (2014).
20. Morales-Juberias, R., Sayanagi, K. M., Dowling, T. E. & Ingersoll, A. P. Emergence of polar-jet polygons from jet instabilities in a Saturn model. *Icarus* **211**, 1284–1293 (2011).
21. Mied, R. & Lindemann, G. Propagation and Evolution of Cyclonic Gulf-Stream Rings. *J. Phys. Oceanogr.* **9**, 1183–1206 (1979).
22. Chassignet, E. & Cushmanroisin, B. On the Influence of a Lower Layer on the Propagation of Nonlinear Oceanic Eddies. *J. Phys. Oceanogr.* **21**, 939–957 (1991).
23. Chan, J. & Williams, R. Analytical and Numerical-Studies of the Beta-Effect in Tropical Cyclone Motion .1. Zero Mean Flow. *J. Atmos. Sci.* **44**, 1257–1265 (1987).
24. Oruba, L., Lapeyre, G. & Riviere, G. On the Poleward Motion of Midlatitude Cyclones in a Baroclinic Meandering Jet. *J. Atmos. Sci.* **70**, 2629–2649 (2013).
25. Ingersoll, A. & Cuzzi, J. Dynamics of Jupiters Cloud Bands. *J. Atmos. Sci.* **26**, 981-+ (1969).
26. Limaye, S. Jupiter - New Estimates of the Mean Zonal Flow at the Cloud Level. *Icarus* **65**, 335–352 (1986).
27. Li, L. M. *et al.* Life cycles of spots on Jupiter from Cassini images. *Icarus* **172**, 9–23 (2004).
28. Garcia-Melendo, E., Perez-Hoyos, S., Sanchez-Lavega, A. & Hueso, R. Saturn's zonal wind profile in 2004-2009 from Cassini ISS images and its long-term variability. *Icarus* **215**, 62–74 (2011).
29. Dowling, T. A Relationship Between Potential Vorticity and Zonal Wind on Jupiter. *J. Atmos. Sci.* **50**, 14–22 (1993).
30. Rhines, P. Waves and Turbulence on a Beta-Plane. *J. Fluid Mech.* **69**, 417–443 (1975).
31. Kaspi, Y. *et al.* Jupiter's atmospheric jet streams extend thousands of kilometres deep. *Nature* **555**, 223-+ (2018).
32. Galanti, E. Constraints on the latitudinal profile of Jupiter's deep jets. **submitted**, (2021).

33. Heimpel, M., Gastine, T. & Wicht, J. Simulation of deep-seated zonal jets and shallow vortices in gas giant atmospheres. *Nature Geoscience* **9**, 19-+ (2016).

34. Yadav, R. K., Heimpel, M. & Bloxham, J. Deep convection-driven vortex formation on Jupiter and Saturn. *Sci. Adv.* **6**, eabb9298 (2020).

35. Adriani, A. *et al.* JIRAM, the Jovian Infrared Auroral Mapper. *Space Sci. Rev.* **213**, 393–446 (2017).

36. Gonzalez, R. C. & Woods, R. E. *Digital Image Processing*. (Pearson, 2016).

37. Garcia-Ortega, E., Lopez, L. & Sanchez, J. L. Diagnosis and sensitivity study of two severe storm events in the Southeastern Andes. *Atmos. Res.* **93**, 161–178 (2009).

38. Marion, G. R. & Trapp, R. J. The Dynamical Coupling of Convective Updrafts, Downdrafts, and Cold Pools in Simulated Supercell Thunderstorms. *J. Geophys. Res.-Atmos.* **124**, 664–683 (2019).

39. Merrill, R. A Comparison of Large and Small Tropical Cyclones. *Mon. Weather Rev.* **112**, 1408–1418 (1984).

40. Emanuel, K. A. *Atmospheric Convection*. (Oxford University Press, 1994).

41. Marshall, J. & Schott, F. Open-ocean convection: Observations, theory, and models. *Rev. Geophys.* **37**, 1–64 (1999).

42. Little, B. *et al.* Galileo images of lightning on Jupiter. *Icarus* **142**, 306–323 (1999).

43. Gierasch, P. J. *et al.* Observation of moist convection in Jupiter's atmosphere. *Nature* **403**, 628–630 (2000).

44. Gierasch, P., Conrath, B. & Magalhaes, J. Zonal mean properties of Jupiter's upper troposphere from Voyager infrared observations. *Icarus* **67**, 456–483 (1986).

45. Li, L. M., Ingersoll, A. P. & Huang, X. L. Interaction of moist convection with zonal jets on Jupiter and Saturn. *Icarus* **180**, 113–123 (2006).

46. Thomson, S. I. & McIntyre, M. E. Jupiter's Unearthly Jets: A New Turbulent Model Exhibiting Statistical Steadiness without Large-Scale Dissipation*. *J. Atmos. Sci.* **73**, 1119–1141 (2016).

47. Ingersoll, A. P., Bolton, S. J. & Levin, S. M. Vertical momentum transport by atmospheric waves explains Jupiter's stacked, oppositely-rotating Ferrel cells. *Geophysics Research Letters* **Submitted**, (2021).
48. Duer, K., Gavriel, N. & Galanti, E. Evidence for multiple Ferrel cells on Jupiter. *Nature* **submitted**, (2021).
49. Fletcher, L. N. Jupiter's temperate belt/zone contrasts revealed at depth by Juno microwave observations. *J. Geophys. Res.: Planets* **(submitted)**, (2021).
50. Siegelman, L., Klein, P., Ewald, S. P., Ingersoll, A. P. & Young, W. R. Moist convection drives an upscale energy transfer at Jupiter's high latitudes. *Nature* **Submitted**, (2021).
51. Sindoni, G. *et al.* Characterization of the white ovals on Jupiter's southern hemisphere using the first data by the Juno/JIRAM instrument. *Geophys. Res. Lett.* **44**, 4660–4668 (2017).
52. Rubio, A. M., Julien, K., Knobloch, E. & Weiss, J. B. Upscale Energy Transfer in Three-Dimensional Rapidly Rotating Turbulent Convection. *Phys. Rev. Lett.* **112**, 144501 (2014).
53. Novi, L., von Hardenberg, J., Hughes, D. W., Provenzale, A. & Spiegel, E. A. Rapidly rotating Rayleigh-B\'enard convection with a tilted axis. *Phys. Rev. E* **99**, 053116 (2019).
54. Acton, C. H. Ancillary data services of NASA's Navigation and Ancillary Information Facility. *Planet Space Sci.* **44**, 65–70 (1996).

Figures

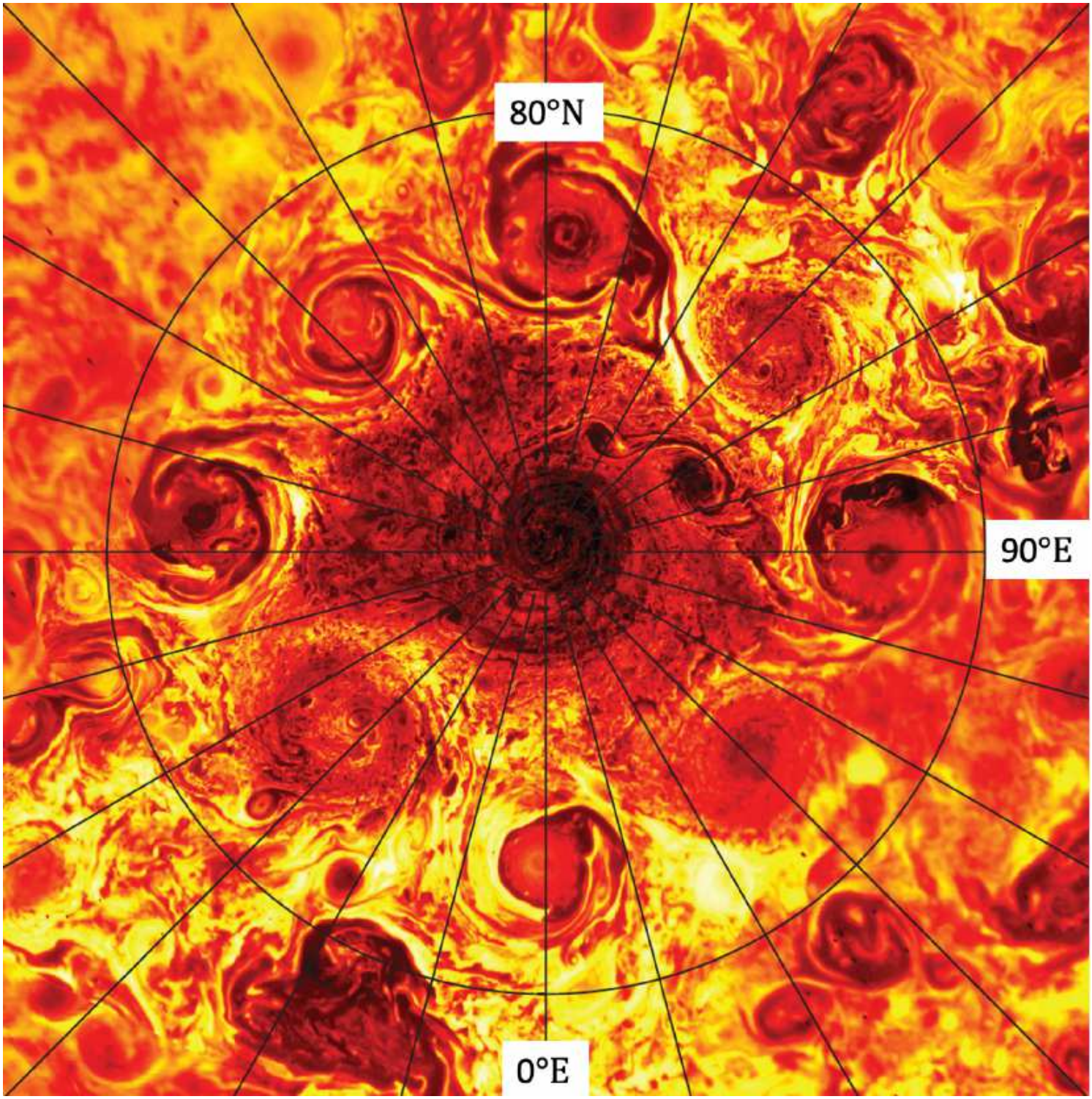

Figure 1

Infrared image of the northern hemisphere as seen by JIRAM 2. The circle at 80° latitude is about 12,000 km from the pole. The radiances have been corrected for nadir viewing, with bright yellow signifying greater radiance and dark red signifying lesser radiance. Because of these corrections and the non-linearity of the Planck function, one can only say that the average brightness temperature is somewhere

in the range 215-220 K. The figures shown in this paper cover the central cyclone and the two cyclones at 135° and 315° east longitude, respectively. The two dark features at 120-150° east, whose filaments spiral toward their centers in a clockwise direction, are anticyclones.

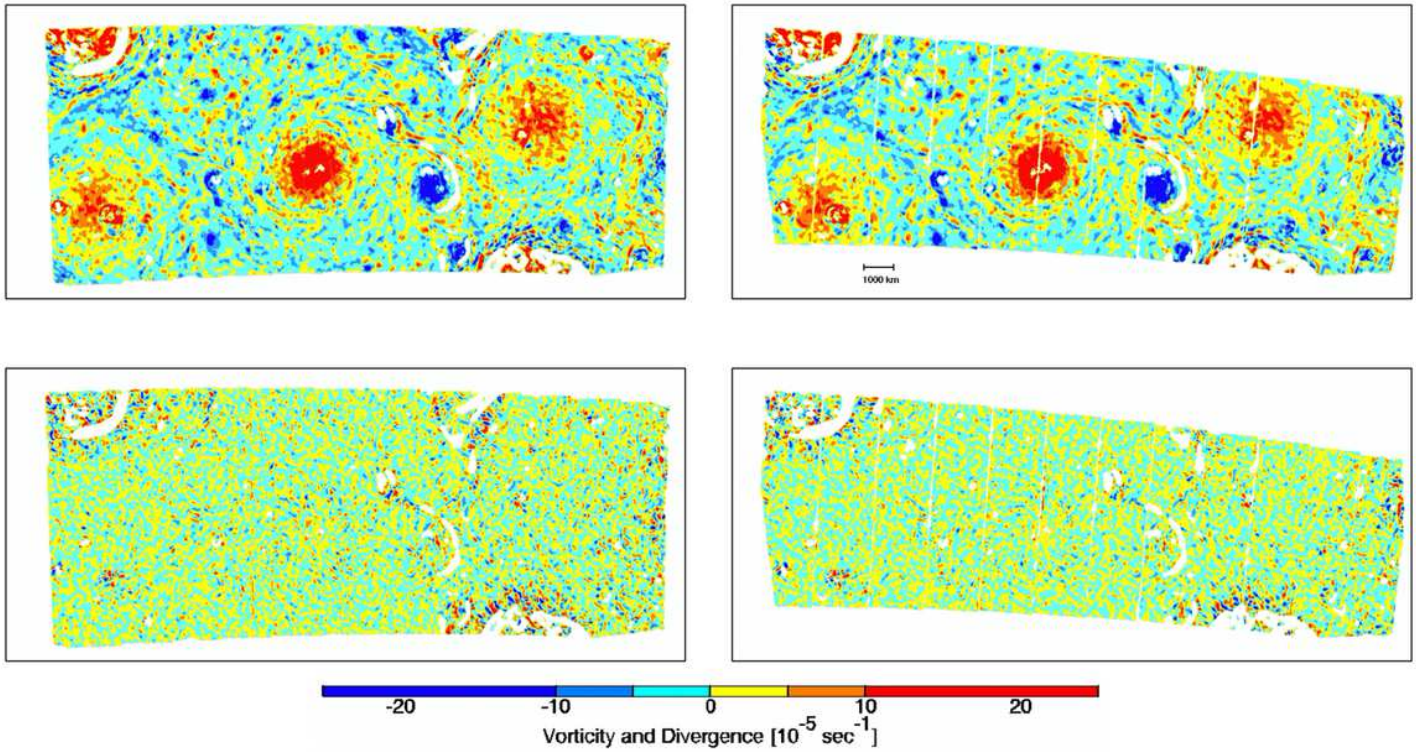

Figure 2

Vorticity (top row) and divergence (bottom row) derived from two determinations of the wind field using separate data (left and right), termed n0103 and n0204. The long dimension of each rectangle is ~20,000 km, and the smallest features are ~100 km in diameter. Each determination is derived from a series, each of which consists of 12 adjacent images laid side by side. The seams between the 12 images are visible as faint vertical lines. The white spaces are regions where the image entropy36 was below a threshold needed for reliable cloud-tracked wind analysis. They cover 1.8% and 2.1% of the pixels in the left and right maps, respectively. For further information, see the Methods section

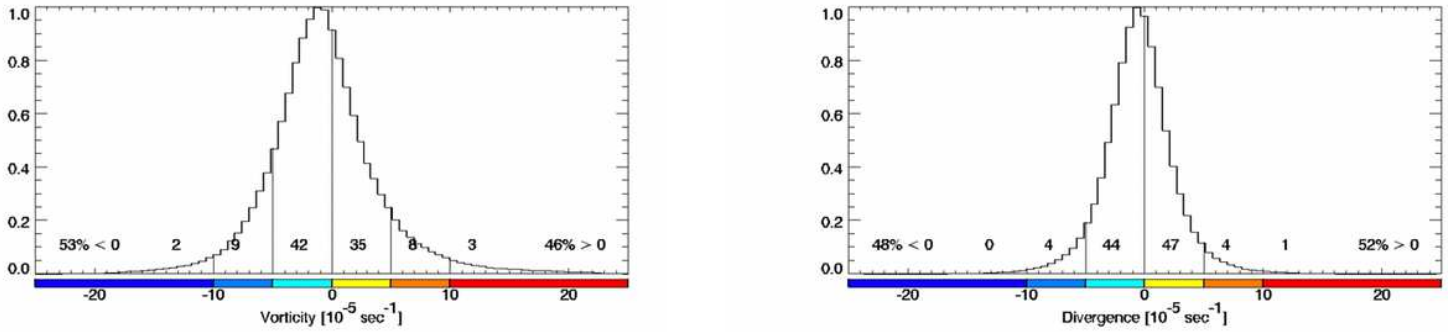

Figure 3

Histograms of vorticity (left) and divergence (right) for the maps shown in Figure 2. The vorticity and divergence scales are the same, and the colors are the same as those used in Figure 2. The number above each color bin is the percentage of pixels in that bin.

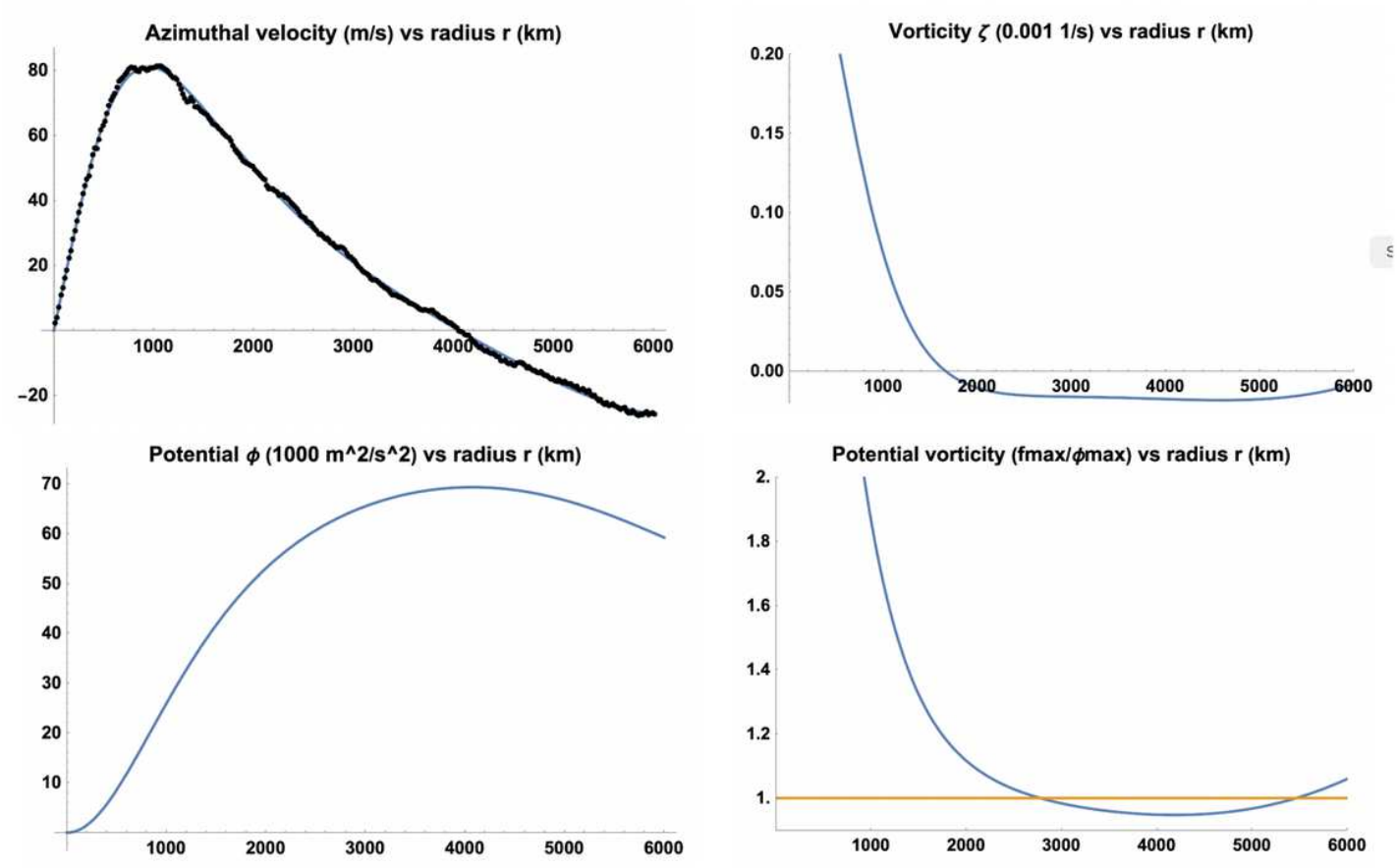

Figure 4

Mean azimuthal velocity and vorticity (top row) and mean gravitational potential and potential vorticity (bottom row). The fitted curve for velocity (blue) is almost covered by the data points (black). Please see manuscript .pdf for full caption.

Supplementary Files

This is a list of supplementary files associated with this preprint. Click to download.

- SupplementaryInformation40221.pdf
- figs1polarvortexblink.pdf
- figs2entropymasksremoved.pdf